https://doi.org/10.5194/egusphere-2025-972
Preprint. Discussion started: 30 April 2025

Multiscale statistical analysis of thermal and non-thermal components of seawater $p\mathrm{CO}_2$ in the Western English Channel: scaling, time-reversibility, and dependence

Kévin Robache and François G. Schmitt

Laboratoire d'Océanologie et Géosciences, Université du Littoral Côte d'Opale, Université de Lille, CNRS, IRD, UMR LOG 8187, F62930 Wimereux, France

Correspondence: Kévin Robache (kevin.robache@univ-littoral.fr) and François G. Schmitt (francois.schmitt@cnrs.fr)

Abstract. The partial pressure of carbon dioxide ($p\mathrm{CO}_2$) has been measured on the ASTAN cardinal buoy (Brittany, west coast of France) with at 30-minute intervals by Gac et al. (2020), yielding a dataset of 32,582 data points collected over a period of nearly five years. These measurements were then coupled with others of sea surface temperature and salinity, chlorophyll a, oxygen saturation and atmospheric pressure. The aim of this study was to consider the statistical properties of the thermal and non-thermal component of $p\mathrm{CO}_2$, based on its relation with temperature established by Takahashi et al. (2009). Using Fourier spectral analysis, it was demonstrated that all marine scalars exhibited scaling properties with power-law slopes ranging from 1.73 to 1.85 for timescales spanning from 12 hours to at least 80-100 days. The results obtained from this analysis indicate a turbulent and intermittent dynamics for all the considered scalars, including sea surface temperature and salinity, chlorophyll a, oxygen saturation, $p\mathrm{CO}_2$, and $p\mathrm{CO}_2$ thermal and non-thermal components. A time-reversibility analysis evidenced the irreversibility of the $p\mathrm{CO}_2$ components above 30 days. The irreversibility exhibited by the thermal component was found to be higher than that of the non-thermal component, with an average value of the associated irreversibility index that was approximately 3.5 times higher than that of the non-thermal component over the period of 50 to 70 days. Furthermore, a methodology known as the Probability Density Function quotient was employed, a method that has not been widely utilized. This approach enabled the identification of values for which there were statistical relationships between variables. This facilitated the quantification of the influence of primary production on the non-thermal $p\mathrm{CO}_2$, or the influence of periods of depression on supersaturation due to atmospheric or terrigenous inputs. This provided new insights into the stochastic coupling between biological and physical processes, when considering high-frequency $p\mathrm{CO}_2$ variability.

1 Introduction

The ocean carbon cycle plays a major role in the global carbon cycle of the Earth. It encompasses a wide array of physico-chemical, biological, and geological processes, each operating at various spatio-temporal scales ranging from the largest to the finest. Examples include extreme events (Yu et al., 2020) and phytoplankton blooms (Bozec et al., 2011). Its significance is crucial for global climate regulation, particularly in light of the pressing issue of global warming. The ocean's role is paramount as it serves as a carbon sink, capable of absorbing approximately 25 % of atmospheric anthropogenic carbon emissions each

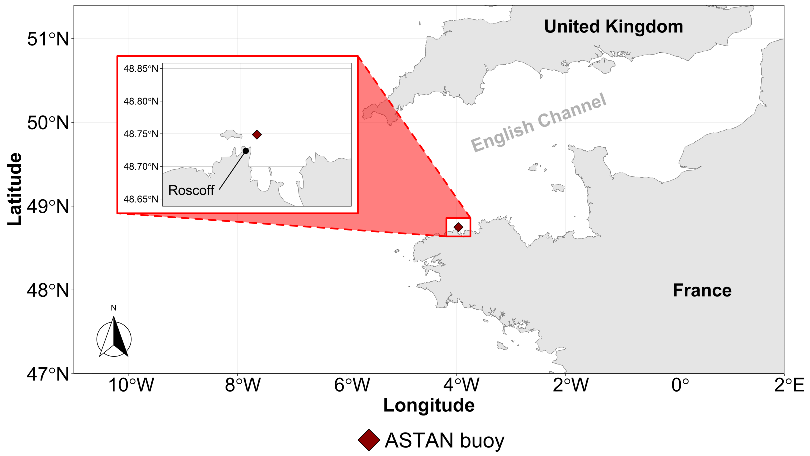

Figure 1. A map of western France indicating the location of the ASTAN buoy off the coast of the city of Roscoff.

year, according to recent estimations (Friedlingstein et al., 2023). To anticipate future dynamics of carbon dioxide (CO_2), models serve as valuable tools, such as those used in the Shared Socio-economic Pathways (SSP) scenarios of the Coupled Model Intercomparison Project Phase 6 (CMIP6) used in the Intergovernmental Panel on Climate Change reports (IPCC; Calvin et al., 2023). However, constructing and/or improving these models requires *in situ* observations (Ciais et al., 2014). Time series analysis, in particular, is needed to assess the multiscale dynamics of monitored quantities. High-frequency time series are therefore essential for constructing reliable models with precise spatial and temporal resolutions. For several years now, efforts are made in this direction to build large observation databases such as the Surface Ocean CO_2 Atlas (SOCAT; Bakker et al., 2016) database, using in part autonomous moorings (Sutton et al., 2014, 2019; Gac et al., 2020). Furthermore, it is really important to record Eulerian (e.g., fixed buoy) or Lagrangian (e.g., drifting buoy) time series to clearly understand the temporal behavior of the marine scalars.

Due to their large variability at all scales, coastal areas are crucial regions to monitor in order to obtain the most accurate carbon balance. These areas are subject to various events having an impact on CO_2 dynamics both in time and space. For example, anthropogenic activities (e.g., industry and agriculture; Northcott et al., 2019), land inputs (Jiang et al., 2013), extreme events (e.g., storms; Crosswell et al., 2014) in these areas are factors of fast CO_2 fluctuations. Furthermore, these zones possess a high seasonality due to different seasonal drivers such as biological activity and sea surface temperature across seasons (Bozec et al., 2011; Marrec et al., 2013; Reimer et al., 2017). Moreover, these areas can also be particularly turbulent. This can impact the variability across different timescales and the properties of the scalars (e.g., reversibility, scaling properties and intermittency; Zongo and Schmitt, 2011; Schmitt and Huang, 2016; Schmitt, 2023) such as seawater CO_2 (Robache et al., 2025). Hence these zones present a complex multiscale variability which needs to be described and understood as far as possible.

Several studies have shown that thermal variations contribute to fluctuations in the partial pressure of CO_2 (pCO_2) at the seawater surface (Takahashi et al., 1993, 2002, 2009; Wanninkhof et al., 2022). However, as previously mentioned, numerous

https://doi.org/10.5194/egusphere-2025-972
Preprint. Discussion started: 30 April 2025

other physical, chemical, biological, and geological events which are not directly linked to temperature dynamics influence the dynamics of $p\mathrm{CO_2}$. These include processes such as photosynthesis and respiration, as well as air-sea $\mathrm{CO_2}$ exchanges (Gac et al., 2020). The variations in the seawater partial pressure of $p\mathrm{CO_2}$ can thus be classified into two groups: thermal and non-thermal components. In this study, we aim to investigate the dynamics of these two components, and to compare them, using statistical tools from the field of turbulent time series analysis. For this, a coastal database situated in the Western English Channel (France) is considered, in order to study an example in a high-variability environment.

The structure of the paper is the following: Sect. 2 presents the data and methods employed in this study, with a detailed description of the approach used to quantify the non-thermal variations of $p\mathrm{CO_2}$ provided in Sect. 2.2. The statistical analysis of these two components is presented in Sect. 3, with a focus on multivariate analysis in Sect. 3.2. Finally, the last sections provide the discussion (Sect. 4) and conclusions (Sect. 5).

2 Data and Methods

2.1 Presentation of the database from the ASTAN cardinal buoy

The data analyzed here belong to the ASTAN cardinal buoy, which is situated off the coast of Brittany, France, within the WEC. Specifically, it is positioned 3.1 km offshore Roscoff (48°44’55” N and 3°57’40” W) as depicted in Fig. 1. The WEC is characterized as a turbulent shallow epicontinental sea (Dauvin, 2019). The average depth at the buoy’s location is 45 m, and this region experiences significant tidal influences, with tidal ranges exceeding 8 m during spring tides (Gac et al., 2020). Consequently, an intense tidal stream is consistently present, facilitating the continuous total vertical mixing of the water column (Pingree and Griffiths, 1978; Reid, 1993; Marrec et al., 2013). This buoy is an integral component of the French national observation service COAST-HF, within the IR-ILICO coastal and marine research infrastructure. The seawater surface partial pressure of $\mathrm{CO_2}$ ($p\mathrm{CO_2}$) data were collected on the buoy using a SAMI-$\mathrm{CO_2}$ (Submersible Autonomous Moored Instrument, SunBurst Sensors) sensor, recording measurements every 30 minutes. This device monitors $p\mathrm{CO_2}$ by detecting pH changes (via absorbance measures) in a bromothymol blue solution contained within a gas-permeable membrane, induced by the presence of $\mathrm{CO_2}$. Sea Surface Temperature (SST) and Sea Surface Salinity (SSS) were simultaneously measured using a SeaBird Inc. SBE16+ sensor, at the same time resolution, and Dissolved Oxygen (DO) and chlorophyll *a* (chl *a*) concentrations were recorded with a SeaBird Inc. SBE43 sensor and a Cyclops7 sensor, respectively (Gac et al., 2020). Oxygen saturation ($\mathrm{O_{sat}}$) was estimated by Gac et al. (2020) following Weiss (1970). Atmospheric pressure ($\mathrm{P_{atm}}$) data were provided by the weather station of the Roscoff Marine Station.

This database was established by Gac et al. (2020); they assessed the dataset’s reliability through a comparison with low-frequency (e.g., weekly) sampling observations with laboratory estimations of $p\mathrm{CO_2}$. The considered database is thus originally composed of six marine and atmospheric parameters ($p\mathrm{CO_2}$, SST, SSS, $\mathrm{O_{sat}}$, chl *a*, $\mathrm{P_{atm}}$) recorded from March 6, 2015 to December 31, 2019 with a time step of 30 minutes. If there were no missing data, the total number of data points would be 84,552. However, due to local failures of the measuring devices, there are missing data for each parameter. Table 1 presents for each parameter the total number of recorded data points, and the associated percentage of missing values: this percentage

Table 1. Number of recorded data points (n) and percentage of missing data ($\%_{\text{missing}}$) for the time series used for the following of this study.

Scalar	n	$\%_{\text{missing}}$
$p\mathrm{CO}_2$	32 582	61.5
Chl a	37 412	55.8
SST	62 981	25.5
SSS	62 475	26.1
O_{sat}	50 752	40.0
P_{atm}	70 483	16.6

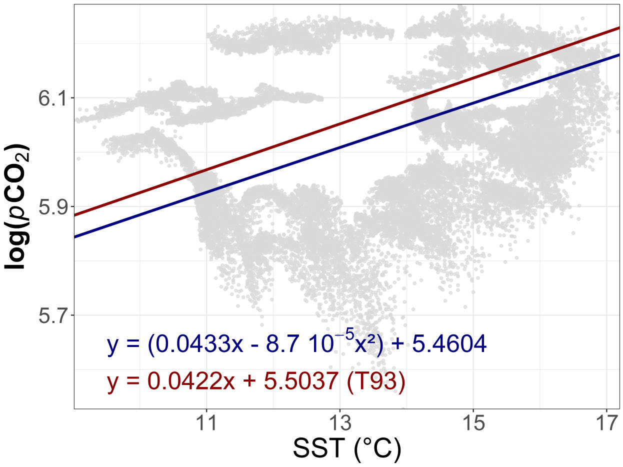

Figure 2. Distribution of the natural logarithm of the $p\mathrm{CO}_2$ data (in μatm) versus the SST (gray points). The empirical linear relation found by Takahashi et al. (1993, T93) is represented by the red line and the red equation. The equation used in this study is represented by the blue line and the blue equation, based on Takahashi et al. (2009).

varies from 16.6 % for P_{atm} to 61.5 % for $p\mathrm{CO}_2$. Due to this large proportion of missing values we are not considering here procedures to fill the gaps. The data analysis methods must then be adapted to time series with large portions of missing values.

2.2 A non-thermal $p\mathrm{CO}_2$ index

We denote $p\mathrm{CO}_2{}^{\text{thermal}}$ the changes of $p\mathrm{CO}_2$ induced by temperature changes, under isochemical conditions. This is written as an exponential relation:

$$p\mathrm{CO}_2{}^{\text{thermal}}(T) = A\exp\left(aT - bT^2\right), \qquad (1)$$

where the parameters classically proposed are the following: $b = 0$ and $a = 0.0423$ °C^{-1} based on North Atlantic seawater data (Takahashi et al., 1993); or $a = 0.0433$ °C^{-1} and $b = 8.7\,10^{-5}$ °C^{-2} from a more recent work using a larger dataset

https://doi.org/10.5194/egusphere-2025-972
Preprint. Discussion started: 30 April 2025

(Takahashi et al., 2009). In the present work, we use the latter relation, but we note that the quadratic term is only providing slight corrections to the linear term. The coefficient A is a multiplicative factor that has no influence on the dynamical or statistical properties of $p\mathrm{CO_2}^{\text{thermal}}$. We estimate this value based on the data, as:

$$A = \left\langle \frac{p\mathrm{CO}_2(t)}{\exp\left(aT(t) - bT(t)^2\right)} \right\rangle, \tag{2}$$

where $\langle\cdot\rangle$ means statistical average, performed on the different values in the time series, where t is the time. When considering the oxygen dynamics in marine waters, one classically divides the oxygen concentration value by the equilibrium oxygen which is a function of temperature and salinity: the ratio is a number without dimension, which is called the oxygen saturation percentage. Inspired by this approach, we consider here the non-thermal dynamics as the ratio X_{sat} between the observed $p\mathrm{CO}_2$ and the thermal component $p\mathrm{CO_2}^{\text{thermal}}$:

$$X_{\text{sat}} = \frac{p\mathrm{CO}_2}{p\mathrm{CO_2}^{\text{thermal}}} \tag{3}$$

This provides a new time series, where $X_{\text{sat}}(t)$ is a non-dimensional quantity, indicating the saturation of $p\mathrm{CO}_2$; it can be seen as a percentage, and when it is larger than 1 (or 100 %) there is super saturation, whereas when smaller than 1 there is under saturation (with respect with an equilibrium value which depends on the temperature).

Let us note that a so-called "non-thermal" component of $p\mathrm{CO}_2$ is often introduced as (Takahashi et al., 1993, 2009; Wimart-Rousseau et al., 2020):

$$p\mathrm{CO_2}^{\text{non-thermal}} = p\mathrm{CO}_2 \times \frac{p\mathrm{CO_2}^{\text{thermal}}(T_{\text{mean}})}{p\mathrm{CO_2}^{\text{thermal}}(T)}, \tag{4}$$

where T_{mean} is the average value of the temperature estimated for a given observation experiment. It can easily be shown using this definition and Eq. (3) that we have $p\mathrm{CO_2}^{\text{non-thermal}} = \lambda X_{\text{sat}}$ with a proportionality coefficient given by $\lambda = p\mathrm{CO_2}^{\text{thermal}}(T_{\text{mean}})$, indicating that the classical expression of the non-thermal $p\mathrm{CO}_2$ is proportional to the saturation value X_{sat} which is considered in the present work. Their dynamics are thus the same, but we prefer here to consider the quantity X_{sat} since it is a non-dimensional quantity and its comparison with the value of 100 % directly indicates supersaturation or undersaturation.

2.3 Fourier spectral analysis

Fourier spectral analysis is used to estimate the spectral dynamics of stationary time series. Due to missing data, the classical Fast Fourier Transform (FFT) algorithm, which needs regularly-space data, cannot be used. We therefore use here the Wiener-Khintchine theorem expressing that the spectral energy density is the Fourier transform of the autocorrelation function $C(\tau) = \langle X(t)X(t+\tau)\rangle$:

$$E(f) = \int_{-\infty}^{+\infty} C(\tau)\exp(-2i\pi\tau f)\mathrm{d}\tau, \tag{5}$$

where f is the frequency, and $E(f)$ is the Fourier spectral energy density. The autocorrelation function can be directly estimated on time series with missing values, hence this algorithm is recommended for estimating the spectral dynamics of such time series. We consider here the code described in Gao et al. (2021). The power spectral density is represented in log-log plot in order to emphasize possible scaling regimes of the form $E(f) \sim f^{-\beta}$, where $\beta > 0$ is the spectral exponent. For Brownian motion, $\beta = 2$, and for passive-scalar turbulence $\beta = 5/3$ (Kolmogorov, 1941; Obukhov, 1949; Corrsin, 1951).

2.4 Time-reversal symmetry

The statistical analysis of time-reversal symmetry allows to assess whether a time series exhibits the same statistical properties when considered in the forward direction of time or in reverse (i.e., by replacing t with $-t$). A time series is considered reversible if its statistical properties remain unchanged regardless of the direction of time. This property was recently studied in the context of turbulence by Schmitt (2023), who observed an increase in time-reversal asymmetry within the inertial turbulent range. This is applied here to *in situ* ocean scalar data, and a time-reversal asymmetry indicator using triple correlations, proposed in the field of statistical physics by Pomeau (Pomeau, 1982, 2004), is used here. This indicator uses the following two triple correlations estimated for a stationary time series u:

$$G^+(\tau) = \frac{\langle u(t)u(t+2\tau)u(t+3\tau)\rangle}{g_3};$$
$$G^-(\tau) = \frac{\langle u(t+3\tau)u(t+\tau)u(t)\rangle}{g_3}, \qquad (6)$$

where $u(t)$ is a zero-mean time series, and $g_3 = \langle u^3 \rangle$ is a normalization, so that G^+ and G^- are dimensionless quantities. The indicator $Po = |G^+ - G^-|$, denoted as the Pomeau index (Schmitt, 2023), quantifies the degree of time-reversal symmetry in a series. For a reversible series, where the direction of time does not affect the triple correlations, $Po = 0$. Conversely, the larger the value of Po, the more the series is asymmetric by time-reversal. Since $Po = 0$ for a reversible series, this indicator is also interpreted here as an indicator of irreversibility in the time series. It can be evaluated for different values of the time increment τ, allowing one to examine how irreversibility varies across scales.

2.5 PDF quotient Q

To analyze the relationship between two random variables, we complement the classical approach of conditional averaging with the Probability Density Function (PDF) quotient method. This method, introduced by Xu et al. (2007), involves estimating the following quotient:

$$Q(x,y) = \log\left(\frac{P_{u,v}(x,y)}{P_u(x)P_v(y)}\right), \qquad (7)$$

where P_u and P_v are the respective PDF of the random variables u and v, and $P_{u,v}(x,y)$ is their joint PDF. This quantity provides insights into the dependence between the two variables in the probability space. Indeed, if u and v are independent, $P_{u,v}(x,y) = P_u(x)P_v(y)$ and so $Q(x,y) = 0$. On the contrary, Q is different from the zero value if a dependence exists. More precisely, $Q > 0$ indicates a positive relation, for which the joint probability density $P_{u,v}(x,y)$ is larger than the product $P_u(x)P_v(y)$ corresponding to the independence between the random variables. Conversely, the values for which $Q < 0$ indicate a “negative” relation, for which the joint probability density is smaller than what would be obtained if the variables were independent.

https://doi.org/10.5194/egusphere-2025-972
Preprint. Discussion started: 30 April 2025

This provides information that complements what is obtained from the correlation. While the correlation is a single numerical value that quantifies the dependence between two variables for all their values (large or small), the PDF quotient reveals which specific values in the (x, y) plane exhibit strong or weak statistical relationships between the variables.

3 Results

3.1 Statistical properties of $p\mathrm{CO_2}^{\mathrm{thermal}}$ and X_{sat} in a turbulence framework

3.1.1 Means and coefficient of variation

The dataset analyzed in this study consists of the original variables given in Table 1 together with the computed series $p\mathrm{CO_2}^{\mathrm{thermal}}$ and X_{sat}. Hence we consider seven key oceanic scalars: the SST, SSS, chl *a*, $\mathrm{O_{sat}}$, $p\mathrm{CO_2}$ and associated thermal ($p\mathrm{CO_2}^{\mathrm{thermal}}$) and non-thermal ($X_{\mathrm{sat}}$) components. First, basic statistical metrics were extracted from these time series, including the mean, standard deviation, and coefficient of variation (CV). These values are presented in Table 2. Most time series exhibit relatively high variability, ranging from 9 % to 17 %. However, three time series fall outside this range. Specifically, SSS and $\mathrm{O_{sat}}$ show lower variability, with CV values of 0.6 % and 4.7 %, respectively. In contrast, the chl *a* time series possesses a much higher CV of 55.6 %, largely due to its strong biological seasonality. Its mean concentration is relatively high, close to 1 μg L^{-1}, which is sometimes observed in highly mesotrophic waters (Simboura et al., 2005). The CV of $p\mathrm{CO_2}$ in this study is smaller than that observed for coastal ocean sites (> 20 %) in our previous work (Robache et al., 2025). Nevertheless, it is noteworthy that the X_{sat} time series still exhibits significant fluctuations, even in this type of environment.

The database was introduced and analyzed in Gac et al. (2020), where various factors influencing the $p\mathrm{CO_2}$ within the Western English Channel (WEC) were identified. These include tidal patterns, daily cycles, specific rainfall events, and biological processes such as respiration and photosynthesis. Expanding on this analysis, the study highlighted the multiscale variability of partial pressure of $\mathrm{CO_2}$ in seawater, spanning timescales from six-hour fluctuations to seasonal trends. Based on these results, here we apply other metrics to characterize the dynamics and inter-relations of these time series.

Table 2. Means (μ), standard deviations (σ) and coefficients of variation ($CV = \sigma/\mu$) for all the time series used in this study.

Scalar (unit)	$\mu \pm \sigma$	CV (%)
$p\mathrm{CO_2}$ (μatm)	416.7 ± 50.1	12.0
X_{sat} (%)	101.0 ± 14.4	14.3
$p\mathrm{CO_2}^{\mathrm{thermal}}$ (μatm)	409.3 ± 37.1	9.1
Chl *a* (μg L^{-1})	0.9 ± 0.5	55.6
SST (°C)	13.1 ± 2.2	16.8
SSS (psu)	35.2 ± 0.2	0.6
$\mathrm{O_{sat}}$ (%)	102.2 ± 4.8	4.7

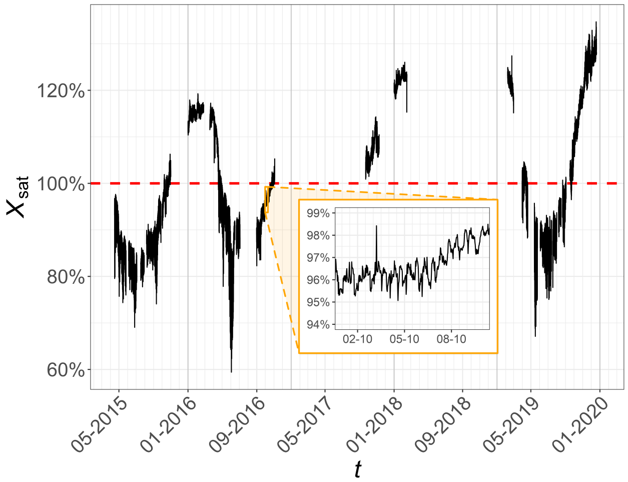

Figure 3. The complete X_{sat} time series, as defined in Eq. (3), represented as a percentage. The red dashed line represents the 100 % value which is reached when $p\text{CO}_2 = p\text{CO}_2{}^{\text{thermal}}$. The inset is a zoom over a period of 10 days showing that the series presents fluctuations even at small scales.

3.1.2 Presentation and distribution of the X_{sat} time series

The time series of X_{sat} is shown in Fig. 3. Notably, this variable does not remain consistently at 100 %, but exhibits significant fluctuations across various timescales, ranging from hours to years. Values vary from a minimum of 59.4 % in June 2016 to a maximum of 134.7 % in December 2019. The mean value is 101.0±14.4 % with a variation coefficient of 14.3 %. In general, this indicates that the non-thermal component of $p\text{CO}_2$ exhibits significant fluctuations, reflecting its own dynamics. At large scale, the values seem to present a seasonal dynamics: X_{sat} is larger than 100 % from October 2015 to April 2016, from September 2017 to February 2018, and from September to December 2019. As already mentioned in Gac et al. (2020), these super-saturated values in winter could be linked with riverine inputs (e.g., from Morlaix and Penzé rivers) and to bacterial respiration. On the contrary, undersaturated X_{sat} values (smaller than 100 %) are found from March to October 2015, from April to October 2016, and from April to September 2019: this corresponds to consumption of CO_2 by the primary production in spring and summer. The PDF of X_{sat} shown in Fig. 4a reflects this seasonal behavior, with peaks between 80 % and 90 % corresponding to primary production, and above 110 % for winter values. Both Figs. 4a-b in linear and log-linear plots respectively show that the PDF is non-Gaussian and also non-symmetric. More values and a longer tail were recorded below 100 %: approximately 55 % of the values are below this threshold according to Fig. 4c.

3.1.3 Scaling properties

Fourier spectra have been estimated for each series and displayed in Fig. 5 in log-log plots. Approximate scaling behavior are found visually; in order to estimate precisely the power-law slopes, power-law regressions are estimated over the same

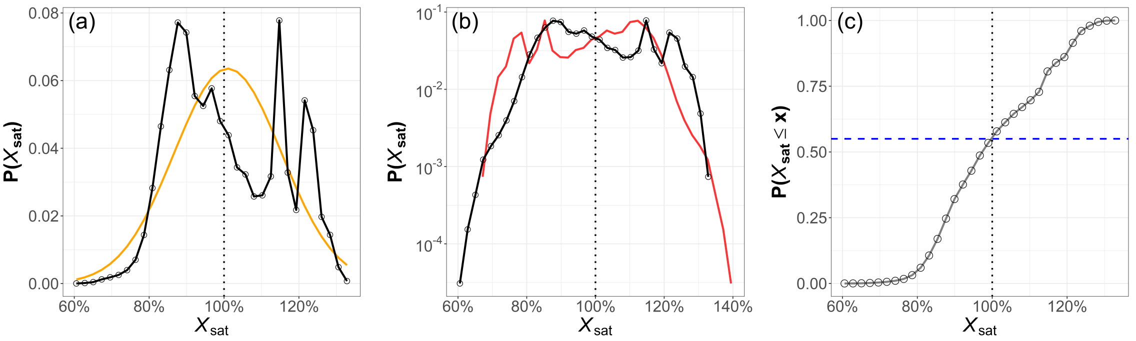

Figure 4. The PDF of X_{sat} time series (%): (a) in linear plot, (b) in log-linear plot and (c) the distribution function. The orange line in (a) shows a Gaussian fit with the same mean and variance; the red line in (b) represents the symmetric PDF; the vertical dashed line in (c) denotes the 100 % value, reached when $p\text{CO}_2 = p\text{CO}_2{}^{\text{thermal}}$ and the horizontal blue line represents the probability $P(X_{\text{sat}} \leq 100) = 0.55$. The band width used in (a) and (b) corresponds to 3 % of the difference between the maximum and minimum values of X_{sat}.

range of scales for each series, from 1.1 (to avoid the daily cycle influence) to 80 days. The values of β and their regression standard deviation area provided in Table 3. In most cases the power-law fits estimated over this range of frequency scales extend approximately over low frequencies until the annual time scale. Additionally, distinct peaks were observed linked to tidal cycles (≈ 12.4 hours in the WEC), and the daily cycle (especially for chl a, Fig. 5d), and annual patterns.

All the slopes are close to the value of 5/3 corresponding to passive scalar turbulence, with values ranging between 1.73 and 1.85. The shapes of the $p\text{CO}_2{}^{\text{thermal}}$ (Fig. 5c) and SST (Fig. 5e) spectra appeared very similar, with the same scaling exponents. The scalars which are usually defined as passive scalars (i.e. SST and SSS; Corrsin, 1951) possess here the smallest β values: the spectral slopes for X_{sat}, $p\text{CO}_2$, O_{sat} and chl a time series are closer to 1.80. This difference with the theoretical $5/3$ value could be explained by a strong small-scale intermittency for these scalars (Frisch, 1995; Seuront et al., 1996). To assess this potential effect, we estimate the fraction of small-scale variance arising from fluctuations below the 12.4 hour tidal scale, using a 12.5-hour moving average. This smoothing procedure reduced high-frequency variability, effectively removing structures with periods shorter than 12.4 h. We then quantified the variance associated with these high-frequency fluctuations by computing the ratio between the variance of the smoothed ($\sigma^2_{\text{smoothed}}$) and original ($\sigma^2$) time series, expressed as a percentage:

$$\rho = 1 - \frac{\sigma^2_{\text{smoothed}}}{\sigma^2} \tag{8}$$

For small values of ρ, the contribution of small-scale variability is limited, whereas larger values of ρ indicate a greater proportion of small-scale fluctuations. As shown in Fig. 6, the steepness of the slope β may be related to the indicator ρ, showing that a relationship emerges between this index of small-scale variability and the value of β.

3.1.4 Reversibility

The reversibility analysis has been applied to all seven time series. An example of triple correlation function G is displayed in Fig. 7 for the SST series only, as an illustration: it is seen that the two functions $G^+(\tau)$ and $G^-(\tau)$ are close for scales τ below

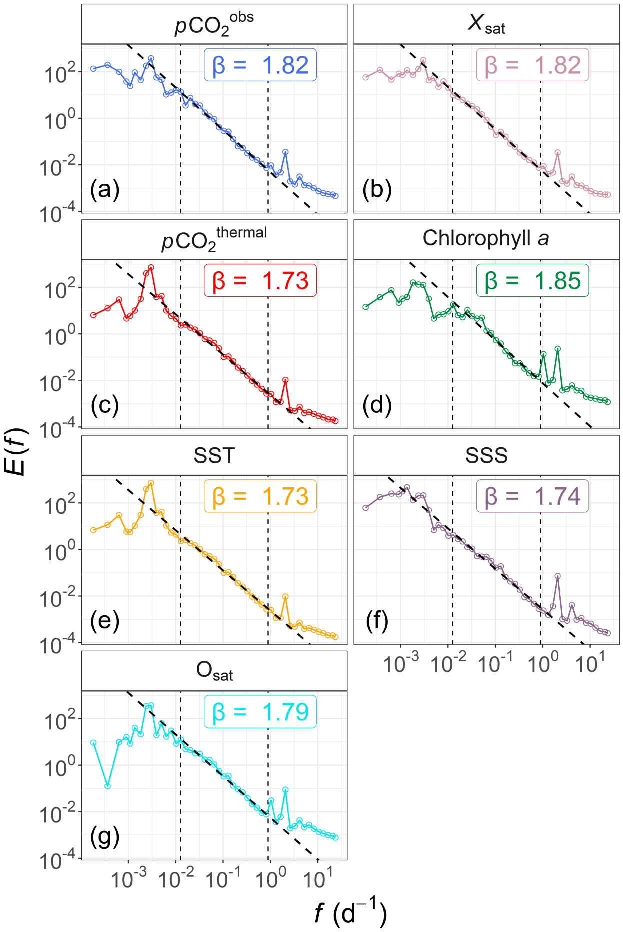

Figure 5. Fourier power spectral analysis, in log-log plots, of seven time series from the ASTAN buoy: (a) $p\mathrm{CO}_2$, (b) X_{sat}, (c) $p\mathrm{CO}_2^{\mathrm{thermal}}$, (d) chlorophyll a, (e) SST, (f) SSS and (g) $\mathrm{O}_{\mathrm{sat}}$. The frequencies are expressed in day^{-1}. The black dashed lines represent the power-law regression for each time series, estimated for frequencies from 1.1 to 80 days. More information about the slopes β associated to these spectra is given in Table 3.

25 days, and after this time scale, the two curves diverge quickly. The corresponding indicator *Po* has low values below this threshold, indicating a time reversibility for this temporal range, and irreversibility after 25 days, as shown in Fig. 8. In this figure all values of $Po(\tau)$ for scales from 0 to 70 days are superposed, since this indicator is dimensionless: it corresponds to a quantification of the departure from 0 of the time-reversal symmetry of each series. We can see that for three series, the curves stays very close to zero at all scales: SSS, chl a and $\mathrm{O}_{\mathrm{sat}}$. These series may be considered as time-reversal symmetric. For the other series, for scales below 30 days, the indicator remains very small, with values smaller than 2, an arbitrary threshold we have plotted in the figure. It is then increasing and reaching an approximate plateau (with fluctuations) for scales from 50 to 70 days.

Table 3. Spectral slopes β estimated for the seven considered parameters, for scales from 1 to 80 days. The associated spectra are displayed in Fig. 5. Difference between each slope values β and β_{SST} are also given to quantify the difference with the passive scalar slope.

Scalar	β	$\beta - \beta_{\mathrm{SST}}$
$p\mathrm{CO}_2$	1.82 ± 0.05	0.09
X_{sat}	1.82 ± 0.04	0.09
$p\mathrm{CO}_2{}^{\mathrm{thermal}}$	1.73 ± 0.05	0
Chl *a*	1.85 ± 0.08	0.12
SST	1.73 ± 0.04	0
SSS	1.74 ± 0.05	0.01
$\mathrm{O}_{\mathrm{sat}}$	1.79 ± 0.05	0.06

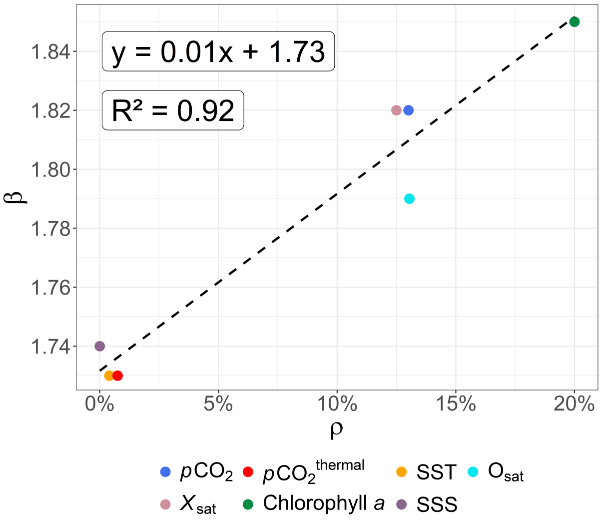

Figure 6. Fourier slope β versus the indicator ρ, representing the influence of high-frequency fluctuations below tidal timescale for each time series. The black dashed line represents a linear regression.

We then consider in Table 4 several values derived from the $Po(\tau)$ curves: the time scale $\tau_{\min}$ corresponding to the first time for which $Po(\tau) > 2$ (for three series this value cannot be extracted since the curve always remains close to zero); the maximal value $Po_{\max}$ reached by Po; and $\overline{Po}$, the average value of Po estimated over scales $\tau \in [50;70]$. This shows that the four series $p\mathrm{CO}_2$, X_{sat}, $p\mathrm{CO}_2{}^{\mathrm{thermal}}$ and SST become clearly irreversible for timescales larger than 30 to 50 days, the larger value $\tau_{\min} = 50.7$ is for the X_{sat} time series. Further, $Po_{\max}$ as well as $\overline{Po}$ are the larger for the $p\mathrm{CO}_2$ time series, followed by $p\mathrm{CO}_2{}^{\mathrm{thermal}}$, SST and X_{sat} in decreasing order. As for the Fourier spectra, it can be seen that SST and $p\mathrm{CO}_2{}^{\mathrm{thermal}}$ Po time series dynamics are very similar.

https://doi.org/10.5194/egusphere-2025-972
Preprint. Discussion started: 30 April 2025

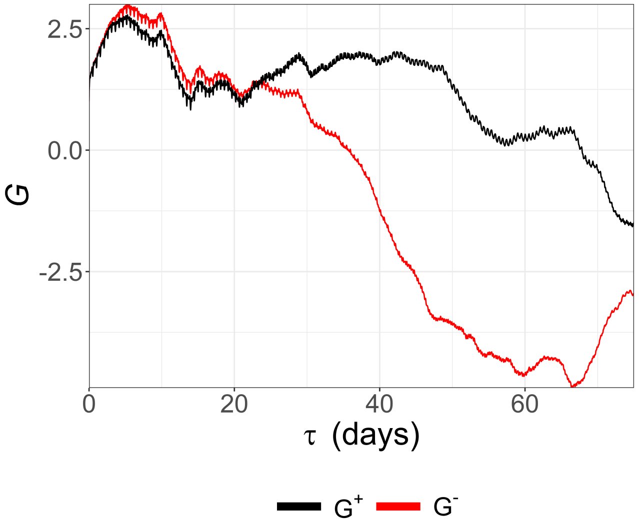

Figure 7. Triple correlation functions $G^+(\tau)$ (black line) and $G^-(\tau)$ (red line) for the SST time series.

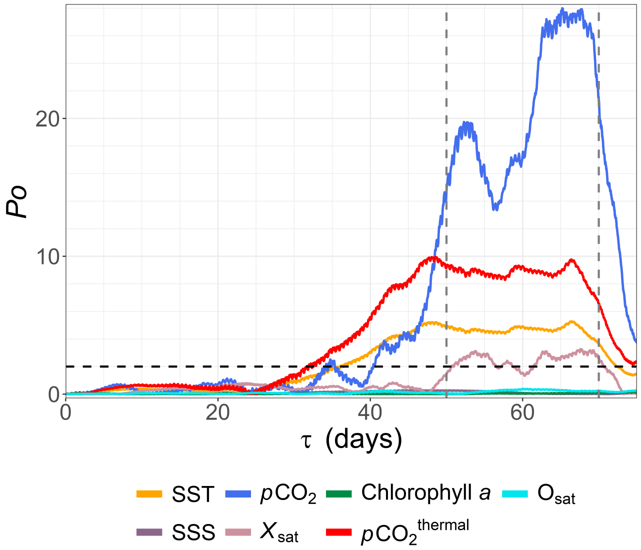

Figure 8. The indicator Po versus τ for all seven time series. The horizontal dashed line represents the value $Po = 2$. The vertical dashed lines represent the values $\tau = 50$ and $\tau = 70$ days.

In summary, there are two types of dynamics: chl a, SSS and O_{sat} are found to be time-reversal symmetric, whereas the 220 other series are time-reversal symmetric for scales below one month, and become irreversible for larger scales, the stronger irreversibility being found for $p\mathrm{CO}_2$ and $p\mathrm{CO}_2{}^{\mathrm{thermal}}$.

Table 4. The minimum value $\tau_{\min}$ for which *Po* > 2; the maximum value of *Po*, and the mean $\overline{Po}$ and standard deviation of *Po* estimated for $\tau \in [50; 70]$ for each scalar.

Scalar	$\tau_{\min}(Po \geq 2)$ (days)	$Po_{\max}$	$\overline{Po} \pm \sigma$
$p\text{CO}_2$	34.2	28.0	20.9 ± 4.9
$p\text{CO}_2{}^{\text{thermal}}$	31.6	9.9	8.8 ± 0.5
SST	36.1	5.3	4.7 ± 0.3
X_{sat}	50.7	3.0	2.5 ± 0.5
Chl *a*	-	0.2	-
SSS	-	0.3	-
O_{sat}	-	0.4	-

3.2 Multivariate statistics

3.2.1 Conditional means

In this subsection and the following the focus is directly on the behavior of X_{sat}. We consider here first the conditional means of X_{sat} with respect to the values of other variables, to visualize the interactions between variables. They are displayed in Fig. 9. First, three plots show a direct and clear relation. There is as expected a direct relation between $p\text{CO}_2$ and X_{sat} visible in Fig. 9d. Further, a clear relation is also observed between the chl *a* concentration and X_{sat} in Fig. 9e: an increase in the former is linked with a decrease in the latter. The same relation is observed in Fig. 9f, suggesting that it may be the effect of primary production and thus of the oceanic biological carbon pump.

Furthermore, a link between X_{sat} and SSS is also noted, however less clear for large values of SSS, in Fig. 9b: low salinity values are linked to high values of X_{sat}. A similar relationship is found with atmospheric pressure P_{atm} in Fig. 9c: large values of X_{sat} are found in case of atmospheric depressions. These two observations suggest an effect of rainfall events and/or river discharges, which impact $p\text{CO}_2$. This quantitatively confirms what was visually mentioned in Gac et al. (2020).

Finally, a link is also found between SST and X_{sat} in Fig. 9a. This observation may seem counterintuitive due to the definition of X_{sat}, in which $p\text{CO}_2$ is corrected from direct temperature influences. However, the pattern in Fig. 9a can be explained by indirect influences: on the one hand, there is the annual seasonality of SST and on the other hand, there are different seasonal processes impacting $p\text{CO}_2$ without having a direct link with temperature dynamics, such as phytoplankton blooms during spring or significant rainfall events and storms during autumn and winter. Moreover, this association is primarily linked to the seasonality of biological activity, as demonstrated in Fig. 10. Indeed, the two time series presented in Fig. 10a appear to have an opposite dynamics: their Pearson correlation yields a value of -0.84 (with a p-value $\approx 1\ 10^{-12}$). The monthly seasonality is also depicted in Fig. 10b, where the two time series appear to have seasonal averages that are clearly related through a seasonal elongated lemniscate.

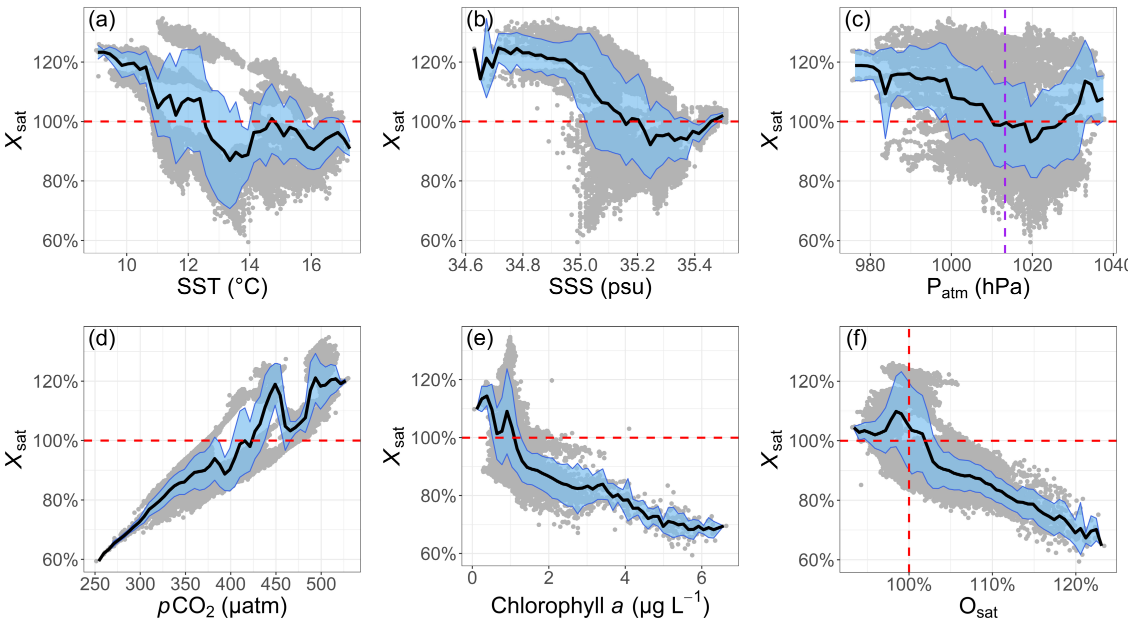

Figure 9. Conditional means of $X_{\text{sat}}(t)$ with respect to several other variables: (a) SST, (b) SSS, (c) atmospheric pressure P_{atm}, (d) $p\text{CO}_2$, (e) chlorophyll *a* and (f) oxygen saturation O_{sat}. The blue area represents the standard deviation calculated for each range. The red vertical dashed lines—and the horizontal one in panel (f)—represent the 100 % value. The purple vertical dashed line in panel (c) represent the mean atmospheric pressure at mean sea level (1013.25 hPa). For each variable, the chosen bandwidth b_w used for the calculation of the conditional mean is defined as 2 % of the difference between its maximum and minimum values. The x-value is the mean of each bounds of each range.

3.2.2 PDF quotient $Q(x,y)$

In this subsection, the statistical relations of X_{sat} with other parameters is considered using the PDF quotient method. The results are presented in Fig. 11, with blue and red colors for negative and positive values of $Q(x,y)$, respectively. Let us recall here that regions for which $Q > 0$ indicate values for which there are strong statistical relationships between the variables and when $Q = 0$ there are no statistical relations between the variables. Low values of Q are emphasized by gray zones (for which $|Q| < 0.2$). They correspond to an lack of statistical relationship as found for a large part of the panel (c) for atmospheric pressure, or of panel (b) for SSS. On the contrary red values show large relationships. Table 5 shows the minimum and maximum values of the PDF quotient for each parameter. This range shows that the minimum values are close for each parameter, and that the maximum values is much larger for $p\text{CO}_2$, chl *a* and O_{sat} (with values from $10^{4.1} \simeq 12{,}600$ to $10^{4.5} \simeq 31{,}600$) than for SST, SSS or P_{atm} (with values from $10^{2.1} \simeq 125$ to $10^{2.3} \simeq 200$). Such large values indicate a strong statistical relationship. More comments are provided below as related with the values of X_{sat}.

We first consider the half-plane for which $X_{\text{sat}} < 100$ %: panel (e) shows that large Q values are observed for large chl *a* (> 2 μg L^{-1}) and low X_{sat} values (< 85 %), and panel (f) similarly that large Q values are found for large O_{sat} (> 110 %) and

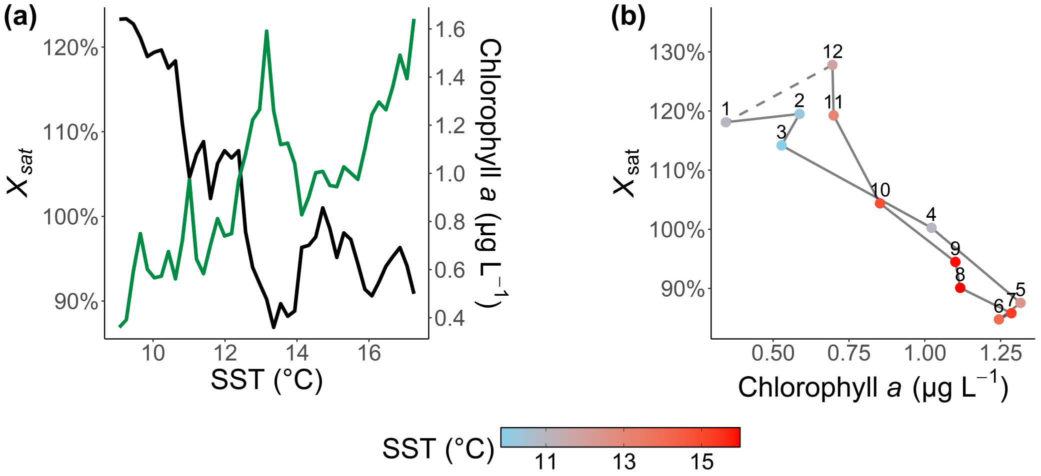

Figure 10. Illustration of the link between X_{sat} and the seasonality of the chlorophyll a: (a) conditional means of chlorophyll a (green line) and X_{sat} (black line) versus the SST (as in Fig. 9) and (b) mean X_{sat} versus the mean chlorophyll a (black line). The color of the dots indicates the mean SST for each month of the year themselves indicated by numbers (1 for January, 12 for December).

low $p\text{CO}_2$ (< 350 μatm) values. This corresponded to phytoplankton bloom periods, during which low X_{sat} values are reached due to CO_2 consumption associated with photosynthesis: the PDF quotient method is a way to provide a quantification that confirms visual observations. The links between chl a and X_{sat} are more complex for values below 2 μg L^{-1}, with Q values closer to 0. In some cases, a "negative" relation ($Q < 0$) can even be found. More globally, an independency ($Q = 0$) or a lower relation ($|Q| < 1$) was more often observed for this range of chl a values, which are more often recorded referring to the associated joint probabilities (97 % of the chl a recorded values).

For intermediate values of X_{sat} (between 85 % and 115 %, representing 64 % of recorded data), the patterns are often mixed. The mean values of Q for this X_{sat} range of values were globally all smaller than 1 and even close to zero in some cases, e.g. with chl a for X_{sat} values ranging between 100 and 105 % (Fig. 11e). This is especially true between 85 % and 95 %, where no clear link is observed with any other scalar, visible by the gray zones in the figures. For X_{sat} values between 95 % and 105 %, larger values of Q are found for $\text{O}_{\text{sat}} < 95$ %.

Finally, let us consider large values of X_{sat} (> 115 %), for which large Q values are observed for the lower part of the SSS values (below 35 psu) in panel (b), and below 1000 hPa for the pressure in panel (c). The two observations are consistent and indicate that supersaturation of X_{sat} corresponds to a depression with lower values of salinity due to rainfall or riverine inputs. In panel (a) the lower temperatures associated with large values of Q indicate that such events happen in winter. Here also the PDF quotient approach helps to quantify relationships and to provide a quantitative justification of proposed mechanisms.

https://doi.org/10.5194/egusphere-2025-972
Preprint. Discussion started: 30 April 2025

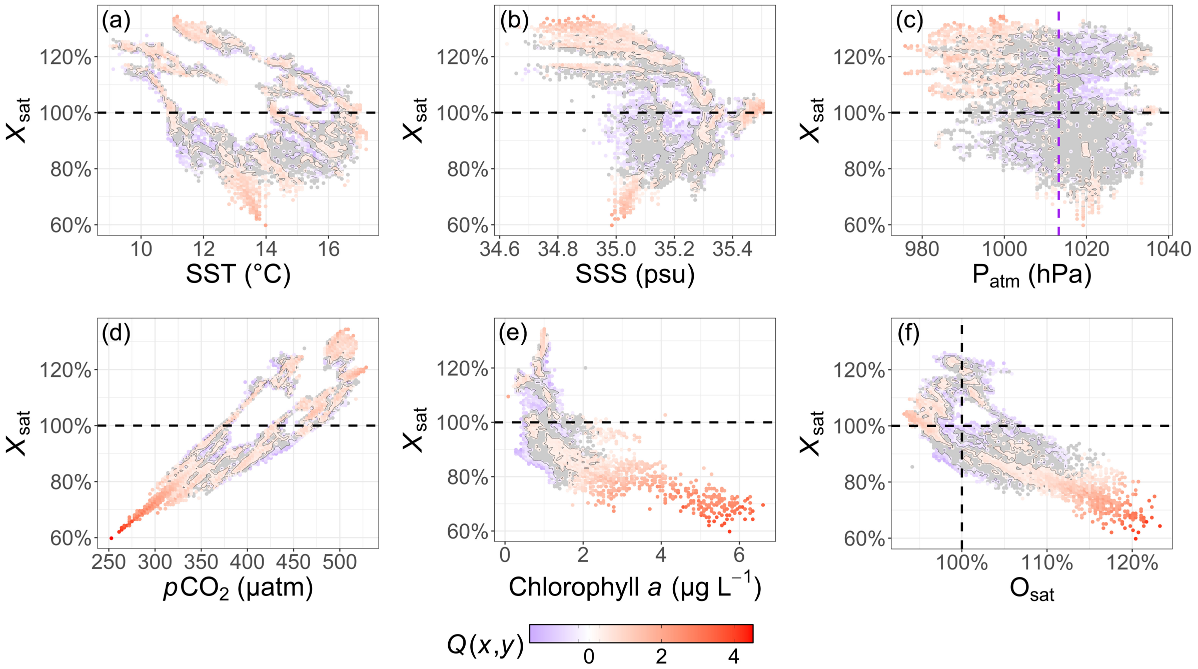

Figure 11. Representation of the PDF quotient $Q(x, y)$ estimated for X_{sat} and (a) SST, (b) SSS, (c) atmospheric pressure P_{atm}, (d) $p\text{CO}_2$, (e) chlorophyll a and (f) oxygen saturation O_{sat}. The horizontal black dashed lines—and the horizontal one in panel (f)—represent the 100 % value. The vertical purple dashed line in panel (c) represents the mean atmospheric pressure at mean sea level (1013.25 hPa). For each variable, the chosen bandwidth used for the calculation of the 2D-PDF is defined as 1 % of the difference between its maximum and minimum values. The x-value and y-value are the mean of each bounds of each range. A contour plot of the value $|Q| = 0.3$ is represented in each panel and the value below this threshold are represented in gray, to separate visually the area where $10^Q < 2$.

Table 5. The minimum and maximum values of the PDF quotient Q for each scalar in comparison to X_{sat}.

Scalar	Q_{min}	Q_{max}
SST	-1.3	2.1
SSS	-1.4	2.2
P_{atm}	-1.2	2.3
$p\text{CO}_2$	-1.6	4.5
Chl a	-1.6	4.1
O_{sat}	-1.5	4.2

https://doi.org/10.5194/egusphere-2025-972
Preprint. Discussion started: 30 April 2025

4 Discussion

The time series recorded on the ASTAN cardinal buoy have been used to study the statistical properties of several marine scalars, of which the thermal and non-thermal components of the seawater partial pressure of $\mathrm{CO_2}$. First, a quantity, X_{sat}, was proposed in Eq. (3), similar to $p\mathrm{CO_2}^{\text{non-thermal}}$ found in the literature (Takahashi et al., 1993, 2009; Wimart-Rousseau et al., 2020) but proportional to it. The advantage of using X_{sat} is that it provides a $p\mathrm{CO_2}$ saturation percentage, allowing for the direct identification of sources (supersaturation) or sinks (undersaturation). For the database studied here, X_{sat} primarily ranges between 80 (5th percentile $= 81$ %) and 120 % (95th percentile $= 124$ %).

In this work, we focused on X_{sat} and its relationship with other measured quantities. All marine quantities studied are influenced by turbulence, exhibiting scale-invariant statistics with a spectral exponent β close to 5/3 (Fig. 5) over timescales ranging from 12 hours to at least 80-100 days. In certain time series, annual, daily, and especially tidal forcing were evident. For some series, the β values were larger than the 5/3 Kolmogorov-Obukhov-Corrsin passive scalar value corresponding to non-intermittent turbulence. This has already been found for SST and chl *a* in a previous study in the Eastern English Channel (Seuront et al., 1996). The slightly steeper slopes found for some series could be related with the intermittency, as supported by the link observed between the importance of the high-frequency fluctuations, below the tidal forcing timescale ($\simeq 12.4$ h) on the scalar dynamics and the associated β values found (Fig. 6). Remarkably, the 5/3 slope was also observed for X_{sat}. This indicates that even without thermodynamic effects, oceanic $p\mathrm{CO_2}$ dynamics in the WEC remains influenced by turbulence. This result differs from our previous study, where we found a mean power-law slope of 1.47 for coastal seawater time series (Robache et al., 2025). This discrepancy could be attributed to the strong hydrodynamic forcing in the present dataset, primarily driven by the macrotidal dynamics of the WEC (tidal range > 4 m; Levoy et al., 2000; Idier et al., 2012).

Despite these similarities in spectral slopes, the time series exhibit different dynamics, as revealed by the reversibility analysis through the time reversal symmetry analysis. Interestingly, quantities more closely linked to biology, such as $\mathrm{O_{sat}}$ and chl *a*, and even SSS, are reversible, despite their otherwise turbulent dynamics. Other quantities are reversible at small scales and become irreversible at timescales greater than 30 days. At these larger timescales, we found that the most irreversible signals are those of $p\mathrm{CO_2}$ and $p\mathrm{CO_2}^{\text{thermal}}$. The quantity X_{sat} exhibits an intermediate behavior between SST, $p\mathrm{CO_2}$, and the reversible variables, as if accounting for the direct effects of temperature had brought it closer to biological dynamic. The fact that some series become irreversible at scales larger than 30 to 50 days could be related to climate forcing. Indeed, irreversibility in climate time series has already been observed by Giancaterini et al. (2022). Moreover, we applied Empirical Mode Decomposition, an algorithm that extracts modal fluctuations from a time series (Huang et al., 1998), to SST (not shown here). This analysis revealed that irreversibility may be associated with large-scale modal fluctuations, including those with periods of one year or longer.

The relation between variables have been investigated for X_{sat}, with the conditional mean and PDF quotient methods. The conditional means, and especially the PDF quotients, have made it possible to quantify the observation first made visually on the X_{sat} series. For low values of X_{sat}, the conditional mean, as well as the PDF quotient, showed that these values are associated with high values of chl *a* and O_{sat}, showing that they are associated with photosynthesis and primary production at temperatures

https://doi.org/10.5194/egusphere-2025-972
Preprint. Discussion started: 30 April 2025

between 12 and 14 °C. High X_{sat} values are often associated with low atmospheric pressures, lower SSS values (visible through the PDF quotient) and, for some of them, lower temperature values ($<$ 12 °C). This indicates that these supersaturation episodes are found during depressions associated with rainfall (atmospheric inputs) and rivers. Another interesting result was the finding of a indirect effect of SST on X_{sat}, due to the links between SST and other parameters influencing the non-thermal component of CO_2 such as chl a. The PDF quotient is a novel methodology that was proposed in the past (Xu et al., 2007), yet it has received limited utilization since its inception. In this study, we have employed the PDF quotient method in a systematic manner to augment the conventional bivariate conditional mean analysis. The PDF quotient approach has enabled us to identify the values in the (x, y) space of the variables under investigation where the statistical relationship is most robust. This approach is also noteworthy for its ability to highlight areas in the (x, y) space where statistical independence exists, i.e. values of Q close to zero, as illustrated in gray in Fig. 11. For example, it is evident from Fig. 11 that atmospheric pressure shows no correlation with X_{sat}, except in one quadrant where X_{sat} has high values and simultaneously the pressure is low, as illustrated in panel (c). This also shows that salinity exhibits no relationship with X_{sat}, except in areas of low salinity and high X_{sat} values, as shown in panel (b). Furthermore, it can also be seen that when X_{sat} assumes slightly undersaturated values (between 90 and 100 $\%$), all the figures corresponding to the PDF quotient associated with different quantities are grayed out, indicating that the PDF quotient approaches zero for these values of X_{sat}. This observation demonstrates that these slightly undersaturated non-thermal $p\text{CO}_2$ values exhibit no discernible relationship with any variable; the underlying causes are multifaceted, and no single parameter appears to be determinative. This is in contrast to the behavior observed for low or very high trans values of X_{sat}, as previously discussed.

The methodological framework used in this study highlights the importance of advanced statistical tools for analyzing fixed-point time series, particularly in highly non-linear and turbulent environments such as WEC. The combination of spectral, time-reversal symmetry, and conditional dependence (conditional means and PDF quotient) analysis has allowed us to study and better understand the complex and scale-dependent dynamics of several scalars and of their relation. The non-linear nature of oceanic $p\text{CO}_2$ dynamics is evident in the interplay between physical, chemical and biological processes, which influence the variability of X_{sat} and $p\text{CO}_2{}^{\text{thermal}}$ in a non-linear way across different timescales.

This study also underscores the necessity of considering non-linear dynamics and interactions when analyzing air-sea CO_2 fluxes and identifying source-sink dynamics, as the dynamics of $\Delta p\text{CO}_2$ is highly linked to oceanic $p\text{CO}_2$ one (Robache et al., 2025). The emergence of different behaviors at various temporal scales—such as reversibility at small scales and increasing irreversibility beyond 30–50 days—suggests that deterministic and stochastic influences act differently across timescales in the WEC carbon cycle. This confirms the complex nature of oceanic carbon dynamics and fluxes and underscores the necessity of high-frequency, robust statistical analyses to fully capture and understand them.

5 Conclusions

Fixed-point measurements, collected via high-frequency buoys, are of critical importance for the study of coastal marine dynamics. They also provide a theoretical framework for interpreting fluctuations, as demonstrated here through the application of Eulerian turbulence. For this, high frequency is necessary in order to access the dynamics at small scales, a necessity due to the presence of strong multiscale fluctuations in the systems under study. In this context, a novel quantity, designated X_{sat}, was considered, with its properties evaluated in relation to the other variables. This quantity directly allows $p\mathrm{CO}_2$ of the direct thermal part to be corrected, and highlights periods of supersaturation or undersaturation linked to non-thermal events. We were thus able to highlight here the influence of turbulence on the different parameters, including the X_{sat} quantity, for scales between 1 day and 80-100 days. Our results also highlight a marked irreversibility in $p\mathrm{CO}_2$ time series above 30 days, suggesting the influence of non-stationary and dissipative processes, likely linked to underlying oceanic and atmospheric dynamics. This temporal turbulent and asymmetric dynamics has implications for $p\mathrm{CO}_2$ modeling and forecasting, emphasizing the need for approaches that account for irreversible fluctuations and turbulent transport mechanisms in the ocean and atmosphere.

In addition, we explored the potential of a little-known method, the PDF quotient, which makes it possible to identify values for which variables have statistical relationships between them. This enabled us to quantitatively analyze visual observations, such as the influence of primary production on the value of X_{sat} (for X_{sat} below 85 %), or the influence of periods of depression on supersaturation (for X_{sat} above 115 %) due to atmospheric or terrigenous inputs. This method provided new insights into the stochastic coupling between biological and physical processes, reinforcing the importance of considering both drivers when interpreting high-frequency $p\mathrm{CO}_2$ variability. Furthermore, this analysis confirms the complex relationship between $p\mathrm{CO}_2$ and other variables considered as its drivers, such as chlorophyll *a* which can serve as a proxy for the biological carbon pump, emphasizing the need for deeper investigations into their statistical causal relations.

Finally, the findings of this study have direct potential applications in oceanographic monitoring and carbon cycle research. The methodology developed here enhances the accuracy of oceanic $p\mathrm{CO}_2$ dynamics analysis, providing a more precise characterization of high-frequency variability. This improved characterization contributes to a better understanding of coastal biogeochemical processes across multiple temporal scales—an essential step, for example, toward verifying and improving model-based forecasts.

Code and data availability. The used database was provided by Gac et al. (2020). The code for the Fourier spectral analysis is based on Gao et al. (2021): https://github.com/lanlankai/Scaling-Analysis-of-the-CFOSAT-Along-Track-Wind-and-Wave-Data. All the plots have been made using the 'ggplot2' (https://doi.org/10.32614/CRAN.package.ggplot2), other 'tidyverse' (https://doi.org/10.32614/CRAN.package.tidyverse; Wickham et al., 2019), and 'ggmagnify' (https://github.com/hughjonesd/ggmagnify; Hugh-Jones, 2023) R packages.

Author contributions. KR performed the code and the analysis under the supervision of FGS. KR wrote the first draft and both authors edited and reviewed the final version.

Competing interests. The authors declare that no competing interests are present.

Acknowledgements. The French Région Hauts-de-France and the ANR project CO_2Coast (principal investigator Hubert Loisel, grant no. ANR-20-CE01-0021) are acknowledged for cofunding of the PhD thesis of Kévin Robache.

Financial support. This research has been supported by the Région Hauts-de-France and by the Agence Nationale de la Recherche (grant no. ANR-20-CE01-0021).

References

Bakker, D. C. E., Pfeil, B., Landa, C. S., Metzl, N., O'Brien, K. M., Olsen, A., Smith, K., Cosca, C., Harasawa, S., Jones, S. D., Nakaoka, S.-i., Nojiri, Y., Schuster, U., Steinhoff, T., Sweeney, C., Takahashi, T., Tilbrook, B., Wada, C., Wanninkhof, R., Alin, S. R., Balestrini, C. F., Barbero, L., Bates, N. R., Bianchi, A. A., Bonou, F., Boutin, J., Bozec, Y., Burger, E. F., Cai, W.-J., Castle, R. D., Chen, L., Chierici, M., Currie, K., Evans, W., Featherstone, C., Feely, R. A., Fransson, A., Goyet, C., Greenwood, N., Gregor, L., Hankin, S., Hardman-Mountford, N. J., Harlay, J., Hauck, J., Hoppema, M., Humphreys, M. P., Hunt, C. W., Huss, B., Ibánhez, J. S. P., Johannessen, T., Keeling, R., Kitidis, V., Körtzinger, A., Kozyr, A., Krasakopoulou, E., Kuwata, A., Landschützer, P., Lauvset, S. K., Lefèvre, N., Lo Monaco, C., Manke, A., Mathis, J. T., Merlivat, L., Millero, F. J., Monteiro, P. M. S., Munro, D. R., Murata, A., Newberger, T., Omar, A. M., Ono, T., Paterson, K., Pearce, D., Pierrot, D., Robbins, L. L., Saito, S., Salisbury, J., Schlitzer, R., Schneider, B., Schweitzer, R., Sieger, R., Skjelvan, I., Sullivan, K. F., Sutherland, S. C., Sutton, A. J., Tadokoro, K., Telszewski, M., Tuma, M., van Heuven, S. M. A. C., Vandemark, D., Ward, B., Watson, A. J., and Xu, S.: A Multi-Decade Record of High-Quality $f\mathrm{CO_2}$ Data in Version 3 of the Surface Ocean $\mathrm{CO_2}$ Atlas (SOCAT), Earth System Science Data, 8, 383–413, https://doi.org/10.5194/essd-8-383-2016, 2016.

Bozec, Y., Merlivat, L., Baudoux, A. C., Beaumont, L., Blain, S., Bucciarelli, E., Danguy, T., Grossteffan, E., Guillot, A., Guillou, J., Répécaud, M., and Tréguer, P.: Diurnal to Inter-Annual Dynamics of $p\mathrm{CO_2}$ Recorded by a CARIOCA Sensor in a Temperate Coastal Ecosystem (2003–2009), Marine Chemistry, 126, 13–26, https://doi.org/10.1016/j.marchem.2011.03.003, 2011.

Calvin, K., Dasgupta, D., Krinner, G., Mukherji, A., Thorne, P. W., Trisos, C., Romero, J., Aldunce, P., Barrett, K., Blanco, G., Cheung, W. W., Connors, S., Denton, F., Diongue-Niang, A., Dodman, D., Garschagen, M., Geden, O., Hayward, B., Jones, C., Jotzo, F., Krug, T., Lasco, R., Lee, Y.-Y., Masson-Delmotte, V., Meinshausen, M., Mintenbeck, K., Mokssit, A., Otto, F. E., Pathak, M., Pirani, A., Poloczanska, E., Pörtner, H.-O., Revi, A., Roberts, D. C., Roy, J., Ruane, A. C., Skea, J., Shukla, P. R., Slade, R., Slangen, A., Sokona, Y., Sörensson, A. A., Tignor, M., Van Vuuren, D., Wei, Y.-M., Winkler, H., Zhai, P., Zommers, Z., Hourcade, J.-C., Johnson, F. X., Pachauri, S., Simpson, N. P., Singh, C., Thomas, A., Totin, E., Arias, P., Bustamante, M., Elgizouli, I., Flato, G., Howden, M., Méndez-Vallejo, C., Pereira, J. J., Pichs-Madruga, R., Rose, S. K., Saheb, Y., Sánchez Rodríguez, R., Ürge-Vorsatz, D., Xiao, C., Yassaa, N., Alegría, A., Armour, K., Bednar-Friedl, B., Blok, K., Cissé, G., Dentener, F., Eriksen, S., Fischer, E., Garner, G., Guivarch, C., Haasnoot, M., Hansen, G., Hauser, M., Hawkins, E., Hermans, T., Kopp, R., Leprince-Ringuet, N., Lewis, J., Ley, D., Ludden, C., Niamir, L., Nicholls, Z., Some, S., Szopa, S., Trewin, B., Van Der Wijst, K.-I., Winter, G., Witting, M., Birt, A., Ha, M., Romero, J., Kim, J., Haites, E. F., Jung, Y., Stavins, R., Birt, A., Ha, M., Orendain, D. J. A., Ignon, L., Park, S., Park, Y., Reisinger, A., Cammaramo, D., Fischlin, A., Fuglestvedt, J. S., Hansen, G., Ludden, C., Masson-Delmotte, V., Matthews, J. R., Mintenbeck, K., Pirani, A., Poloczanska, E., Leprince-Ringuet, N., and Péan, C.: IPCC, 2023: Climate Change 2023: Synthesis Report. Contribution of Working Groups I, II and III to the Sixth Assessment Report of the Intergovernmental Panel on Climate Change [Core Writing Team, H. Lee and J. Romero (Eds.)]. IPCC, Geneva, Switzerland., Tech. rep., Intergovernmental Panel on Climate Change (IPCC), 2023.

Ciais, P., Dolman, A. J., Bombelli, A., Duren, R., Peregon, A., Rayner, P. J., Miller, C., Gobron, N., Kinderman, G., Marland, G., Gruber, N., Chevallier, F., Andres, R. J., Balsamo, G., Bopp, L., Bréon, F.-M., Broquet, G., Dargaville, R., Battin, T. J., Borges, A., Bovensmann, H., Buchwitz, M., Butler, J., Canadell, J. G., Cook, R. B., DeFries, R., Engelen, R., Gurney, K. R., Heinze, C., Heimann, M., Held, A., Henry, M., Law, B., Luyssaert, S., Miller, J., Moriyama, T., Moulin, C., Myneni, R. B., Nussli, C., Obersteiner, M., Ojima, D., Pan, Y., Paris, J.-D., Piao, S. L., Poulter, B., Plummer, S., Quegan, S., Raymond, P., Reichstein, M., Rivier, L., Sabine, C., Schimel, D., Tarasova, O., Valentini, R., Wang, R., van der Werf, G., Wickland, D., Williams, M., and Zehner, C.: Current Systematic Carbon-Cycle Observations and the Need for Implementing a Policy-Relevant Carbon Observing System, Biogeosciences, 11, 3547–3602, https://doi.org/10.5194/bg-11-3547-2014, 2014.

Corrsin, S.: On the Spectrum of Isotropic Temperature Fluctuations in an Isotropic Turbulence, Journal of Applied Physics, 22, 469–473, https://doi.org/10.1063/1.1699986, 1951.

Crosswell, J. R., Wetz, M. S., Hales, B., and Paerl, H. W.: Extensive CO_2 Emissions from Shallow Coastal Waters during Passage of Hurricane Irene (August 2011) over the Mid-Atlantic Coast of the U.S.A, Limnology and Oceanography, 59, 1651–1665, https://doi.org/10.4319/lo.2014.59.5.1651, 2014.

Dauvin, J.-C.: Chapter 6 - The English Channel: La Manche, in: World Seas: An Environmental Evaluation (Second Edition), edited by Sheppard, C., pp. 153–188, Academic Press, ISBN 978-0-12-805068-2, 2019.

Friedlingstein, P., O'Sullivan, M., Jones, M. W., Andrew, R. M., Bakker, D. C. E., Hauck, J., Landschützer, P., Le Quéré, C., Luijkx, I. T., Peters, G. P., Peters, W., Pongratz, J., Schwingshackl, C., Sitch, S., Canadell, J. G., Ciais, P., Jackson, R. B., Alin, S. R., Anthoni, P., Barbero, L., Bates, N. R., Becker, M., Bellouin, N., Decharme, B., Bopp, L., Brasika, I. B. M., Cadule, P., Chamberlain, M. A., Chandra, N., Chau, T.-T.-T., Chevallier, F., Chini, L. P., Cronin, M., Dou, X., Enyo, K., Evans, W., Falk, S., Feely, R. A., Feng, L., Ford, D. J., Gasser, T., Ghattas, J., Gkritzalis, T., Grassi, G., Gregor, L., Gruber, N., Gürses, Ö., Harris, I., Hefner, M., Heinke, J., Houghton, R. A., Hurtt, G. C., Iida, Y., Ilyina, T., Jacobson, A. R., Jain, A., Jarníková, T., Jersild, A., Jiang, F., Jin, Z., Joos, F., Kato, E., Keeling, R. F., Kennedy, D., Klein Goldewijk, K., Knauer, J., Korsbakken, J. I., Körtzinger, A., Lan, X., Lefèvre, N., Li, H., Liu, J., Liu, Z., Ma, L., Marland, G., Mayot, N., McGuire, P. C., McKinley, G. A., Meyer, G., Morgan, E. J., Munro, D. R., Nakaoka, S.-I., Niwa, Y., O'Brien, K. M., Olsen, A., Omar, A. M., Ono, T., Paulsen, M., Pierrot, D., Pocock, K., Poulter, B., Powis, C. M., Rehder, G., Resplandy, L., Robertson, E., Rödenbeck, C., Rosan, T. M., Schwinger, J., Séférian, R., Smallman, T. L., Smith, S. M., Sospedra-Alfonso, R., Sun, Q., Sutton, A. J., Sweeney, C., Takao, S., Tans, P. P., Tian, H., Tilbrook, B., Tsujino, H., Tubiello, F., van der Werf, G. R., van Ooijen, E., Wanninkhof, R., Watanabe, M., Wimart-Rousseau, C., Yang, D., Yang, X., Yuan, W., Yue, X., Zaehle, S., Zeng, J., and Zheng, B.: Global Carbon Budget 2023, Earth System Science Data, 15, 5301–5369, https://doi.org/10.5194/essd-15-5301-2023, 2023.

Frisch, U.: Turbulence: The Legacy of A. N. Kolmogorov, Cambridge University Press, ISBN 978-0-521-45713-2, 1995.

Gac, J.-P., Marrec, P., Cariou, T., Guillerm, C., Macé, É., Vernet, M., and Bozec, Y.: Cardinal Buoys: An Opportunity for the Study of Air-Sea CO_2 Fluxes in Coastal Ecosystems, Frontiers in Marine Science, 7, https://doi.org/10.3389/fmars.2020.00712, 2020.

Gao, Y., Schmitt, F. G., Hu, J., and Huang, Y.: Scaling Analysis of the China France Oceanography Satellite Along-Track Wind and Wave Data, Journal of Geophysical Research: Oceans, 126, e2020JC017 119, https://doi.org/10.1029/2020JC017119, 2021.

Giancaterini, F., Hecq, A., and Morana, C.: Is Climate Change Time-Reversible?, Econometrics, 10, 36, https://doi.org/10.3390/econometrics10040036, 2022.

Huang, N. E., Shen, Z., Long, S. R., Wu, M. C., Shih, H. H., Zheng, Q., Yen, N.-C., Tung, C. C., and Liu, H. H.: The Empirical Mode Decomposition and the Hilbert Spectrum for Nonlinear and Non-Stationary Time Series Analysis, Proceedings of the Royal Society of London. Series A: Mathematical, Physical and Engineering Sciences, 454, 903–995, https://doi.org/10.1098/rspa.1998.0193, 1998.

Hugh-Jones, D.: Ggmagnify: Create a Magnified Inset of Part of a "Ggplot" Object, 2023.

Idier, D., Dumas, F., and Muller, H.: Tide-Surge Interaction in the English Channel, Natural Hazards and Earth System Sciences, 12, 3709–3718, https://doi.org/10.5194/nhess-12-3709-2012, 2012.

Jiang, L.-Q., Cai, W.-J., Wang, Y., and Bauer, J. E.: Influence of Terrestrial Inputs on Continental Shelf Carbon Dioxide, Biogeosciences, 10, 839–849, https://doi.org/10.5194/bg-10-839-2013, 2013.

https://doi.org/10.5194/egusphere-2025-972
Preprint. Discussion started: 30 April 2025

Kolmogorov, A. N.: On Degeneration (Decay) of Isotropic Turbulence in an Incompressible Viscous Liquid, in: Dokl. Akad. Nauk SSSR, vol. 31, pp. 538–540, 1941.

Levoy, F., Anthony, E. J., Monfort, O., and Larsonneur, C.: The Morphodynamics of Megatidal Beaches in Normandy, France, Marine Geology, 171, 39–59, https://doi.org/10.1016/S0025-3227(00)00110-9, 2000.

Marrec, P., Cariou, T., Collin, E., Durand, A., Latimier, M., Macé, E., Morin, P., Raimund, S., Vernet, M., and Bozec, Y.: Seasonal and Latitudinal Variability of the CO_2 System in the Western English Channel Based on Voluntary Observing Ship (VOS) Measurements, Marine Chemistry, 155, 29–41, https://doi.org/10.1016/j.marchem.2013.05.014, 2013.

Northcott, D., Sevadjian, J., Sancho-Gallegos, D. A., Wahl, C., Friederich, J., and Chavez, F. P.: Impacts of Urban Carbon Dioxide Emissions on Sea-Air Flux and Ocean Acidification in Nearshore Waters, PLOS ONE, 14, e0214 403, https://doi.org/10.1371/journal.pone.0214403, 2019.

Obukhov, A. M.: The Structure of the Temperature Field in a Turbulent Flow, IZv. Akad. Nauk SSSR. Ser. Geogr. Geofia, 13, 1949.

Pingree, R. D. and Griffiths, D. K.: Tidal Fronts on the Shelf Seas around the British Isles, Journal of Geophysical Research: Oceans, 83, 4615–4622, https://doi.org/10.1029/JC083iC09p04615, 1978.

Pomeau, Y.: Symétrie des fluctuations dans le renversement du temps, Journal de Physique, 43, 859–867, https://doi.org/10.1051/jphys:01982004306085900, 1982.

Pomeau, Y.: Time in Science: Reversibility vs. Irreversibility, in: Discrete Integrable Systems, edited by Grammaticos, B., Tamizhmani, T., and Kosmann-Schwarzbach, Y., pp. 425–436, Springer, Berlin, Heidelberg, ISBN 978-3-540-40357-9, 2004.

Reid, P. C.: Quality Status Report of the North Sea 1993: Report on Sub-region 9 : The Channel, North Sea Task Force, 1993.

Reimer, J. J., Cai, W.-J., Xue, L., Vargas, R., Noakes, S., Hu, X., Signorini, S. R., Mathis, J. T., Feely, R. A., Sutton, A. J., Sabine, C., Musielewicz, S., Chen, B., and Wanninkhof, R.: Time Series $p\mathrm{CO}_2$ at a Coastal Mooring: Internal Consistency, Seasonal Cycles, and Interannual Variability, Continental Shelf Research, 145, 95–108, https://doi.org/10.1016/j.csr.2017.06.022, 2017.

Robache, K., Schmitt, F. G., and Huang, Y.: Scaling and Intermittent Properties of Oceanic and Atmospheric $p\mathrm{CO}_2$ Time Series and Their Difference in a Turbulence Framework, Nonlinear Processes in Geophysics, 32, 35–49, https://doi.org/10.5194/npg-32-35-2025, 2025.

Schmitt, F. G.: Scaling Analysis of Time-Reversal Asymmetries in Fully Developed Turbulence, Fractal and Fractional, 7, 630, https://doi.org/10.3390/fractalfract7080630, 2023.

Schmitt, F. G. and Huang, Y.: Stochastic Analysis of Scaling Time Series: From Turbulence Theory to Applications, Cambridge University Press, ISBN 978-1-107-06761-5, 2016.

Seuront, L., Schmitt, F., Lagadeuc, Y., Schertzer, D., Lovejoy, S., and Frontier, S.: Multifractal Analysis of Phytoplankton Biomass and Temperature in the Ocean, Geophysical Research Letters, 23, 3591–3594, https://doi.org/10.1029/96GL03473, 1996.

Simboura, N., Panayotidis, P., and Papathanassiou, E.: A Synthesis of the Biological Quality Elements for the Implementation of the European Water Framework Directive in the Mediterranean Ecoregion: The Case of Saronikos Gulf, Ecological Indicators, 5, 253–266, https://doi.org/10.1016/j.ecolind.2005.03.006, 2005.

Sutton, A. J., Sabine, C. L., Maenner-Jones, S., Lawrence-Slavas, N., Meinig, C., Feely, R. A., Mathis, J. T., Musielewicz, S., Bott, R., McLain, P. D., Fought, H. J., and Kozyr, A.: A High-Frequency Atmospheric and Seawater $p\mathrm{CO}_2$ Data Set from 14 Open-Ocean Sites Using a Moored Autonomous System, Earth System Science Data, 6, 353–366, https://doi.org/10.5194/essd-6-353-2014, 2014.

Sutton, A. J., Feely, R. A., Maenner-Jones, S., Musielwicz, S., Osborne, J., Dietrich, C., Monacci, N., Cross, J., Bott, R., Kozyr, A., Andersson, A. J., Bates, N. R., Cai, W.-J., Cronin, M. F., De Carlo, E. H., Hales, B., Howden, S. D., Lee, C. M., Manzello, D. P., McPhaden, M. J., Meléndez, M., Mickett, J. B., Newton, J. A., Noakes, S. E., Noh, J. H., Olafsdottir, S. R., Salisbury, J. E., Send, U., Trull, T. W.,

https://doi.org/10.5194/egusphere-2025-972
Preprint. Discussion started: 30 April 2025

Vandemark, D. C., and Weller, R. A.: Autonomous Seawater $p\mathrm{CO_2}$ and pH Time Series from 40 Surface Buoys and the Emergence of Anthropogenic Trends, Earth System Science Data, 11, 421–439, https://doi.org/10.5194/essd-11-421-2019, 2019.

Takahashi, T., Olafsson, J., Goddard, J. G., Chipman, D. W., and Sutherland, S. C.: Seasonal Variation of $\mathrm{CO_2}$ and Nutrients in the High-Latitude Surface Oceans: A Comparative Study, Global Biogeochemical Cycles, 7, 843–878, https://doi.org/10.1029/93GB02263, 1993.

Takahashi, T., Sutherland, S. C., Sweeney, C., Poisson, A., Metzl, N., Tilbrook, B., Bates, N., Wanninkhof, R., Feely, R. A., Sabine, C., Olafsson, J., and Nojiri, Y.: Global Sea–Air $\mathrm{CO_2}$ Flux Based on Climatological Surface Ocean $p\mathrm{CO_2}$, and Seasonal Biological and Temperature Effects, Deep Sea Research Part II: Topical Studies in Oceanography, 49, 1601–1622, https://doi.org/10.1016/S0967-0645(02)00003-6, 2002.

Takahashi, T., Sutherland, S. C., Wanninkhof, R., Sweeney, C., Feely, R. A., Chipman, D. W., Hales, B., Friederich, G., Chavez, F., Sabine, C., Watson, A., Bakker, D. C. E., Schuster, U., Metzl, N., Yoshikawa-Inoue, H., Ishii, M., Midorikawa, T., Nojiri, Y., Körtzinger, A., Steinhoff, T., Hoppema, M., Olafsson, J., Arnarson, T. S., Tilbrook, B., Johannessen, T., Olsen, A., Bellerby, R., Wong, C. S., Delille, B., Bates, N. R., and de Baar, H. J. W.: Climatological Mean and Decadal Change in Surface Ocean $p\mathrm{CO_2}$, and Net Sea–Air $\mathrm{CO_2}$ Flux over the Global Oceans, Deep Sea Research Part II: Topical Studies in Oceanography, 56, 554–577, https://doi.org/10.1016/j.dsr2.2008.12.009, 2009.

Wanninkhof, R., Pierrot, D., Sullivan, K., Mears, P., and Barbero, L.: Comparison of Discrete and Underway $\mathrm{CO_2}$ Measurements: Inferences on the Temperature Dependence of the Fugacity of $\mathrm{CO_2}$ in Seawater, Marine Chemistry, 247, 104 178, https://doi.org/10.1016/j.marchem.2022.104178, 2022.

Weiss, R. F.: The Solubility of Nitrogen, Oxygen and Argon in Water and Seawater, Deep Sea Research and Oceanographic Abstracts, 17, 721–735, https://doi.org/10.1016/0011-7471(70)90037-9, 1970.

Wickham, H., Averick, M., Bryan, J., Chang, W., McGowan, L. D., François, R., Grolemund, G., Hayes, A., Henry, L., Hester, J., Kuhn, M., Pedersen, T. L., Miller, E., Bache, S. M., Müller, K., Ooms, J., Robinson, D., Seidel, D. P., Spinu, V., Takahashi, K., Vaughan, D., Wilke, C., Woo, K., and Yutani, H.: Welcome to the Tidyverse, Journal of Open Source Software, 4, 1686, https://doi.org/10.21105/joss.01686, 2019.

Wimart-Rousseau, C., Lajaunie-Salla, K., Marrec, P., Wagener, T., Raimbault, P., Lagadec, V., Lafont, M., Garcia, N., Diaz, F., Pinazo, C., Yohia, C., Garcia, F., Xueref-Remy, I., Blanc, P.-E., Armengaud, A., and Lefèvre, D.: Temporal Variability of the Carbonate System and Air-Sea $\mathrm{CO_2}$ Exchanges in a Mediterranean Human-Impacted Coastal Site, Estuarine, Coastal and Shelf Science, 236, 106 641, https://doi.org/10.1016/j.ecss.2020.106641, 2020.

Xu, H., Ouellette, N. T., and Bodenschatz, E.: Curvature of Lagrangian Trajectories in Turbulence, Physical Review Letters, 98, 050 201, https://doi.org/10.1103/PhysRevLett.98.050201, 2007.

Yu, P., Wang, Z. A., Churchill, J., Zheng, M., Pan, J., Bai, Y., and Liang, C.: Effects of Typhoons on Surface Seawater $p\mathrm{CO_2}$ and Air-Sea $\mathrm{CO_2}$ Fluxes in the Northern South China Sea, Journal of Geophysical Research: Oceans, 125, e2020JC016 258, https://doi.org/10.1029/2020JC016258, 2020.

Zongo, S. B. and Schmitt, F. G.: Scaling Properties of pH Fluctuations in Coastal Waters of the English Channel: pH as a Turbulent Active Scalar, Nonlinear Processes in Geophysics, 18, 829–839, https://doi.org/10.5194/npg-18-829-2011, 2011.